High-resolution infrared spectroscopy of the charge-transfer complex $[Ar-N_2]^{+\cdot}$: A combined experimental/theoretical study

H. Verbraak[a)]
Laser Centre Amsterdam and Department of Physical Chemistry, Vrije Universiteit, De Boelelaan 1083, NL-1081 HV Amsterdam, The Netherlands

J. N. P. van Stralen
Department of Theoretical Chemistry, Vrije Universiteit, De Boelelaan 1083, NL-1081 HV Amsterdam, The Netherlands

J. Bouwman,[a)] J. S. de Klerk, D. Verdes,[b)] and H. Linnartz[a),c),d)]
Laser Centre Amsterdam and Department of Physical Chemistry, Vrije Universiteit, De Boelelaan 1083, NL-1081 HV Amsterdam, The Netherlands

F. M. Bickelhaupt[c),e)]
Department of Theoretical Chemistry, Vrije Universiteit, De Boelelaan 1083, NL-1081 HV Amsterdam, The Netherlands

(Received 22 June 2005; accepted 28 July 2005; published online 10 October 2005)

A combined experimental and theoretical study of the charge-transfer complex $[Ar-N_2]^{+\cdot}$ is presented. Nearly 50 transitions split by spin-rotation interaction have been observed by means of infrared diode laser absorption spectroscopy in a supersonic planar plasma expansion. The band origin is at 2272.2563(18) cm^{-1} and rotational constants in the ground and vibrationally (NN-stretch) excited state amount to 0.128 701(8) cm^{-1} and 0.128 203(8) cm^{-1}, respectively. The interpretation of the data in terms of a charge switch upon complexation is supported by new *ab initio* calculations. The best estimate for a linear equilibrium structure yields $R_e(NN)=1.102$ Å and $R_e(Ar-N)=2.190$ Å. Predictions for molecular parameters not directly available from the experimental results are presented as well. Furthermore, the electronic structure and Ar–N bonding mechanism of $[Ar-N_2]^{+\cdot}$ have been analyzed in detail. The Ar–N bond is a textbook example of a classical 2-center-3-electron bond. © *2005 American Institute of Physics*.
[DOI: 10.1063/1.2039083]

I. INTRODUCTION

Charged complexes and cluster ions have binding energies typically an order of magnitude larger than that found for their neutral van der Waals equivalents. This has been ascribed to the charged nature of the interaction.[1] For high-resolution rovibrational spectroscopic studies this has two consequences: (1) spectra of ionic complexes are generally less dense as intramolecular tunnel motions are largely quenched, but (2) fundamental vibrations can shift as much as several hundred cm^{-1} compared to those known for the uncomplexed species. An illustrative example is the $Ar-HN_2^+$ ionic complex:[2–4] this linear proton bound ionic complex has a binding energy of roughly 2780 cm^{-1} and the NH and NN stretch are found to shift as much as 730 and 217 cm^{-1} with respect to the frequencies observed in free N_2H^+.

An additional problem in studying ionic complexes at high resolution is a controlled formation in large abundances, particularly in direct absorption experiments. This problem is overcome in mass selective vibrational predissociation experiments[5] but also direct absorption experiments have been used successfully in the last years by combining phase-sensitive detection schemes and mass spectrometrically controlled supersonic planar plasma expansions.[6] Just recently, it has been possible with this technique to record rovibrational spectra of the linear "sandwich molecules" $N_2-H^+-N_2$ (Ref. 7) and $[N_2-Ar-N_2]^{+\cdot}$ (Ref. 8) and to compare the experimental results with the outcome of high-level *ab initio* calculations.

A benchmark molecule for studying interactions involving charged fragments is the charge-transfer complex $[Ar-N_2]^{+\cdot}$. This complex is formed very efficiently in Ar/N_2 plasma and has a strong binding energy of roughly 1.2 eV.[9] This may be expected; the Ar and N_2 species have similar ionization potentials (15.760 and 15.581 eV, respectively) and so tend to form a bond with covalent character upon ionic complexation. Upon photodissociation the complex prefers a channel $Ar^{+\cdot}/N_2$, even though $Ar/N_2^{+\cdot}$ should be energetically preferred by 0.18 eV.[10] The latter was explained by showing that a charge switch of the cationic center is induced upon complexation.[11] The present work is a spectroscopic and theoretical extension of the study de-

[a)]Present address: Sackler Laboratory for Astrophysics, Leiden Observatory, Postbus 9513, NL-2300 RA Leiden, The Netherlands.
[b)]Visiting scientist from the Institute of Physical Chemistry, University of Zurich, Winterthurerstrasse 190, CH 8057 Zurich, Switzerland.
[c)]Authors to whom correspondence should be addressed.
[d)]FAX: +31-71-5275819; electronic mail: linnartz@strw.leidenuniv.nl
[e)]FAX: +31-20-5987629; electronic mail: fm.bickelhaupt@few.vu.nl

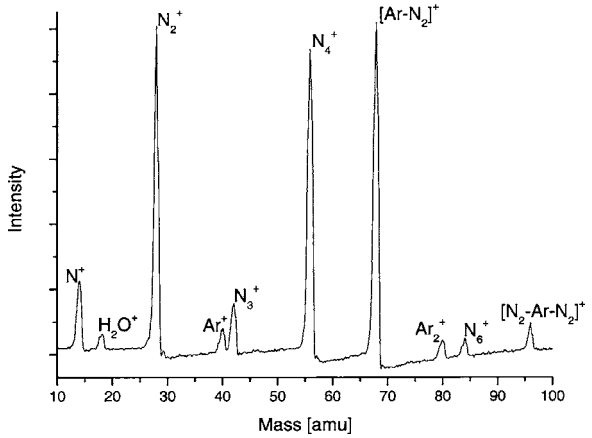

FIG. 1. A mass spectrometric QMS detection of Ar/N_2 plasma generated by electron impact ionization in a supersonic planar plasma expansion.

scribed in the latter reference. High-level *ab initio*[12] and density-functional theory[13,14] (DFT) calculations are presented that confirm the interpretation of the experimental data and predict properties not directly available from the experiment: accurate bond lengths, charge distribution, wave numbers and infrared intensities, the equilibrium rotational constant (B_e), electric-field gradients at the nuclei, and binding energies. Furthermore, the Ar–N bonding mechanism in $[Ar-N_2]^{+\cdot}$ is analyzed using a bond energy decomposition scheme and interpreted in the context of the quantitative molecular orbital (MO) model contained in Kohn-Sham DFT.

II. EXPERIMENTAL AND THEORETICAL METHODS

A. Experimental techniques

The $[Ar-N_2]^{+\cdot}$ cluster ions are generated in a supersonic plasma by electron impact ionization of a gas mixture of 10% N_2 in Ar that is expanded supersonically through a long and narrow slit (3 cm $\times$ 80 μm) with a backing pressure of typically 500 mbars. The radiation of a tunable diode laser multipasses[15,16] the expansion about 3–5 mm downstream and is recorded phase sensitively using lock-in techniques. An effective and fast (10 kHz) production modulation is obtained by periodically changing the electric-field gradients that are used to direct electrons towards the expanding gas. A mass spectrometer is mounted downstream and allows an online characterization of the plasma constituents. This is of importance as optimal production conditions are critical and in addition a large number of quite often rather exotic species is formed in the plasma as well. A mass spectrum of typical Ar/N_2 plasma is shown in Fig. 1. From this figure it becomes clear that besides mixed cluster ions $Ar_nN_m^+$ also pure argon and nitrogen cluster ions are formed. As the experiment is not mass selective, special care has to be taken in identifying spectral features. From the figure one can see that under optimum conditions the $[Ar-N_2]^{+\cdot}$ density is comparable to the N_2^+ density. This reflects the rather large binding energy of the $[Ar-N_2]^{+\cdot}$ ionic complex which is in favor of a straightforward production. The absolute frequency accuracy is of the order of 0.001 cm^{-1} and is achieved by simultaneously recording a reference gas and an etalon spectrum for absolute and relative calibrations, respectively. Details are available from Ref. 6. Recent improvements comprise an updated version of the electron impact source, a larger roots blower system with a total pump capacity of 4500 m^3/h to keep pressures below 0.1 mbar during continuous wave (cw) jet operation and a new software package that allows long scans (1–1.5 cm^{-1}) without loss in spectral accuracy.

B. Theoretical methods

1. Ab initio geometries and energies

Ab initio linear equilibrium structures of $Ar-N_2^{+\cdot}$, N_2, and $N_2^{+\cdot}$ have been optimized using NWCHEM version 4.6,[17] within the spin-unrestricted formalism. Hartree-Fock (HF), Møller-Plesset second-order perturbation theory (MP2), coupled-cluster singles doubles (CCSD), and coupled-cluster singles doubles with noniterative triples [CCSD(T)] have been applied. Hierarchical series of correlation-consistent basis sets[18–21] have been applied to investigate the convergence of the geometries with basis-set size. Our most accurate results are obtained using the CCSD(T) method with the cc-pVQZ basis set.

Binding energies are calculated at geometries that are optimized using the cc-pVQZ basis set. HF, CCSD, and CCSD(T) energy calculations using the cc-pV*X*Z (X=T, Q, and 5) basis sets have been performed. Our most accurate CCSD(T) binding energies are obtained using a basis-set extrapolation of the cc-pVQZ and cc-pV5Z energies. For this purpose we used Eqs. 15.6.1–15.6.3 from the book of Helgaker *et al.*[12] For the energy of the $Ar^{+\cdot}$ ion a spin-orbit coupling (SOC) correction has been calculated using DIRAC.[22] This correction has been calculated by comparing calculated ionization energies of Ar using the full Dirac-Coulomb Hamiltonian and the spin-free Dirac-Coulomb[23] Hamiltonian. The ionization energies have been calculated using the Fock-space CCSD method[24] with an uncontracted cc-pVQZ basis set. Zero-point energy (ZPE) corrections, based on harmonic frequency calculations, have been added to the molecular energies subsequently. In Sec. II B 2 more details about harmonic frequencies are presented.

2. Ab initio vibrational spectra

Harmonic frequencies have been calculated at the CCSD(T)/cc-pVQZ geometry using MP2, CCSD, and CCSD(T) with cc-pVDZ and cc-pVTZ basis sets and for MP2 also with the cc-pVQZ basis set. For MP2/cc-pV*X*Z (X=D,T) and CCSD(T)/cc-pVDZ frequency calculations are also performed at geometries optimized using the corresponding method. Both harmonic and anharmonic CCSD(T)/cc-pVQZ values were estimated for the ν_{N-N} mode of $Ar-N_2^{+\cdot}$ by fitting a fifth-order polynomial to the CCSD(T)/cc-pVQZ energies of 21 points along the harmonic normal mode (in the range of $-0.01-+0.01$ a.u.) obtained at CCSD(T)/cc-pVTZ for the CCSD(T)/cc-pVQZ equilibrium geometry. The quadratic term has been used to approximate the harmonic value at CCSD(T)/cc-pVQZ. The cubic and quartic terms have been used to calculate the corresponding anharmonic correction. The formulas for calculating the anharmonic correction are based on vibrational perturbation

theory and can be found in the literature.[25–27] In our case we only calculated the so-called diagonal correction, i.e., coupling with other modes is neglected. At the MP2 level of theory also infrared intensities have been evaluated.

3. Electric-field gradient calculations

Electric-field gradients (EFGs) on the different nuclei have been calculated using DIRAC. The finite field method with field strengths of ±0.000 01 a.u. has been employed here. The calculations have been performed using the CCSD(T) method with a restricted open-shell Hartree-Fock reference. The spin-free Dirac-Coulomb Hamiltonian has been used here. Since the accurate calculation of EFGs requires the use of extra tight functions to give a proper description of the core regions[28,29] we added an extra tight *s*, *p*, and *d* functions to the uncontracted aug-cc-pVTZ basis set on Ar and N. The values for the exponents of these extra functions have been determined by multiplying the value of the highest exponent with the ratio this value has with the one but highest exponent. So the extra functions have been determined in an even-tempered manner. Nuclear quadrupole coupling constants (NQCC) have subsequently been calculated employing the nuclear quadrupole moment values as tabulated in Ref. 30.

4. DFT geometries, energies, and vibrational spectra

For the DFT calculations we employed the Amsterdam density-functional (ADF) program.[31] All DFT calculations have been performed at both the CCSD(T)/cc-pVQZ geometry and the DFT-optimized geometry.

Geometries, energies, and vibrational spectra have been computed using uncontracted Slater-type orbitals (STOs) without electrons kept frozen. The basis set is a QZ4P set on all atoms. This basis set is of quadruple-ζ quality, augmented with extra polarization functions: two 3*d* and two 4*f* functions on nitrogen and three 3*d* and two 4*f* functions on argon. Ten different density functional have been employed: VWN,[32] VWN including the self-interaction correction from Stoll VWN-Stoll,[33] BP86,[34,35] BLYP,[34,36] PW91,[37,38] PBE,[39,40] revPBE,[41] OPBE,[39,40,42] OLYP,[36,42] and mPW.[38,43]

5. DFT bonding analysis

The bonding mechanism in $[Ar-N_2]^{+\cdot}$ was analyzed using a quantitative bond energy decomposition scheme[44–46] applying ADF. The basis set used for the bonding analysis, TZ2P, is of triple-ζ quality, augmented with two sets of polarization functions on each atom: 3*d* and 4*f* on nitrogen and also 3*d* and 4*f* on argon. The core shells of nitrogen (1*s*) and argon (1*s*2*s*2*p*) were treated using the frozen-core approximation.[47] The overall Ar–N bond energy ΔE is divided into two major components [Eq. (1)]:

$$\Delta E = \Delta E_{\text{prep}} + \Delta E_{\text{int}}. \tag{1}$$

The preparation energy ΔE_{prep} is the amount of energy required to deform the separated fragments from their equilibrium structure to the geometry, which they acquire in the composite molecule. The actual interaction energy ΔE_{int} between the prepared fragments can be further split up into the three physically meaningful terms [Eq. (2)]:

$$\Delta E_{\text{int}} = \Delta V_{\text{elstat}} + \Delta E_{\text{Pauli}} + \Delta E_{\text{oi}}. \tag{2}$$

Here, ΔV_{elstat} corresponds to the classical electrostatic interaction between the unperturbed charge distributions of the prepared fragments *A* and *B* and is usually attractive. The Pauli repulsion ΔE_{Pauli} arises when the energy change associated with the transition from the isolated electron densities $\rho_A+\rho_B$ of the fragments to the wave function $\Psi^0 = N\hat{A}[\Psi_A\Psi_B]$ properly obeys the Pauli principle through explicit antisymmetrization ($\hat{A}$ operator) and renormalization (*N* constant) of the product of fragment wave functions. It comprises the four-electron destabilizing interactions between occupied orbitals and is responsible for any steric repulsion. The orbital interaction ΔE_{oi} accounts for electron-pair bonding, charge transfer (e.g., highest occupied molecular orbital-lowest unoccupied molecular orbital (HOMO-LUMO) interactions), and polarization (empty/occupied mixing on one fragment due to the presence of another fragment).

Furthermore, atomic charges in $[Ar-N_2]^{+\cdot}$ have been calculated using the Voronoi deformation density (VDD) method[48,49] and the Hirshfeld method.[49,50]

III. RESULTS AND DISCUSSION

A. Experimental results

About 100 adjacent vibration-rotation lines have been observed around 2272 cm^{-1} that belong to a progression of *P*- and *R*-branch doublets $[F_1(N), F_2(N)]$ that are due to spin-rotation interaction. Lines due to *Q*-branch transitions lose intensity very rapidly for increasing rotational quantum numbers and are only visible close to the band origin. A weighted stick spectrum of all observed transitions (Ref. 11 and this work) is shown in Fig. 2 and corresponds to a vibrational (NN) excitation within a $^2\Sigma$ state that is due to the mixing of the $3\sigma_g$ molecular orbital of $N_2^{+\cdot}$ with the $3p_\sigma$ (Ar) atomic orbital (see also Sec. III B 3). The Boltzmann profile corresponds to a rotational temperature of about 20 K. The inset shows a typical scan with two subsequent rotational *R*-branch transitions. The spin-rotation splitting amounts to about 0.01 cm^{-1} which is easily resolved and substantially larger than the observed linewidth of 120 MHz [full width at half maximum (FWHM)]. The rotational Hamiltonian is given by $H(^2\Sigma^+) = B_v N^2 - D_v N^4 + \gamma_v SN$ with *N* the rotational quantum number, *S* the total electron spin, and B_v, D_v, and γ_v the rotational, centrifugal distortion, and spin-rotation constant for vibrational level *v*, respectively. Within a Hund's case (b) couplings scheme rotational progressions are described by

$$F_1(N,J) = B_v N(N+1) - D_v N^2(N+1)^2 + \tfrac{1}{2}\gamma_v N \quad \text{for } J = N + \tfrac{1}{2},$$

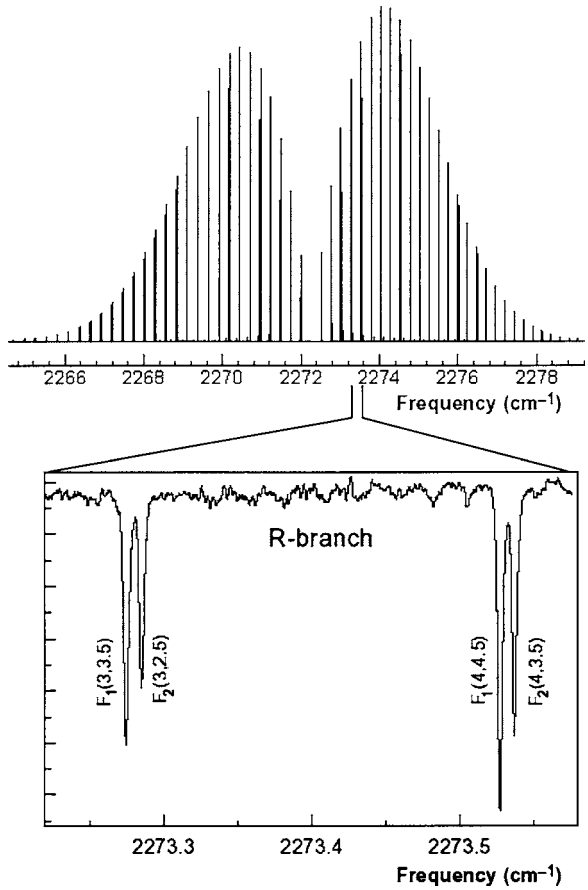

FIG. 2. A weighted overview of all experimentally identified rovibrational transitions of the $[Ar-N_2]^{+\cdot}$ charge-transfer complex. The plot corresponds to a rotational temperature of about 20 K. The inset shows a typical spectrum with transitions split by spin-rotation interaction.

$$F_2(N,J) = B_v N(N+1) - D_v N^2(N+1)^2 - \tfrac{1}{2}\gamma_v(N+1) \quad \text{for } J = N - \tfrac{1}{2},$$

where J is the total angular momentum.

In Fig. 2 transitions with $N=3$ and $N=4$ are shown that split into components $F_1(3.5)/F_2(2.5)$ and $F_1(4.5)/F_2(3.5)$. A complete overview of all available transitions—also two Q-branch transitions—is listed in Table I. In the absence of additional Q-branch transitions that connect levels with different symmetry, it is difficult to distinguish between F_1 and F_2 progressions. However, a comparison of the intensities of two lines in a doublet allows an unambiguous identification as P_1 (and R_1) transitions are stronger than the corresponding P_2 (and R_2) transitions by a factor $N+1/N$. This is particularly clear for low N values that are strongly populated at the low final temperature in the adiabatic expansion. This systematic intensity difference within a doublet is visible from the inset in Fig. 2. All listed transitions are described within a fit routine[51] in which B_v, D_v, and γ_v are determined in the ground $v=0$ and vibrationally excited $v=1$ state. The resulting constants are listed in Table II and—as one may expect—overlap with the conclusions derived in Ref. 11. The corresponding observed-calculated (o-c) values are listed in Table I. The overall accuracy of the fit is better than 0.001 cm^{-1} which is well below the experimental linewidth.

The band origin is found at 2272.2563(2) cm^{-1} which is in between values found for N_4^+ (2234.5 cm^{-1}) (Ref. 52)—in which the charge distribution is delocalized—and $N_2-H^+-N_2$ (2352.2 cm^{-1}) (Ref. 7)—in which the charge is located at the proton—and close to $\nu_{01}=2288.7$ cm^{-1} found for the related centrosymmetric $[N_2-Ar-N_2]^+$ cluster ion.[8] As for the latter case, the charge distribution in $[Ar-N_2]^{+\cdot}$ is expected to be approximately equally distributed over the Ar atom and the complex constituents. This is indeed confirmed by the DFT analyses of the bonding mechanism in Sec. III B 3. The resulting relatively large binding energy is also reflected in the minor change (0.4%) of the rotational constant upon vibrational excitation (Table II).

B. Theoretical results

1. Structure, stability and IR spectrum

The results of our quantum chemical computations are collected in Tables III (benchmark spectroscopic constants) and IV (bonding analysis). For a complete overview of all theoretical results, the reader is referred to Tables S1–S9 in the supplementary material. Our benchmark geometry parameters, obtained at CCSD(T)/cc-pVQZ, are 1.102 Å for the N–N distance and 2.190 Å for the Ar–N distance (Table III). Inspection of Table S2 shows that these values are converged with the basis-set size to within less than 0.01 Å. All DFT methods used in this study reproduce the CCSD(T)/cc-pVQZ benchmark value of the N–N bond distance within a few thousands of angstroms but larger deviations of up to 0.2 Å are found for the Ar–N distance (see Table S2). This is ascribed to the shallow potential-energy surface associated with the Ar–N bond, which causes the equilibrium bond distance to depend more delicately on the level of theory. The CCSD(T)/cc-pVQZ benchmark equilibrium rotational constant B_e agrees well with the experimental B_0: 0.127 50 cm^{-1} versus 0.128 701(8) cm^{-1}. From this it may be concluded that our benchmark geometry is reliable.

The harmonic N–N stretch frequency ν_{N-N} is 2408.2 cm^{-1} at CCSD(T)/cc-pVQZ (see Table III; see also Sec. II B 2). This value still differs by 21 cm^{-1} from the one obtained at CCSD(T)/cc-pVTZ (compare Tables III and S3). The anharmonic correction amounts to −73.7 cm^{-1}, which results in our best estimate for the anharmonic ν_{N-N} of 2334.5 cm^{-1}. Large anharmonicity effects have been observed previously for other complexes as well, e.g., $Ar-HN_2^+$.[4] Note that the discrepancy of 62.2 cm^{-1} between this ν_{N-N} value and the experimental one of 2272.2563(2) cm^{-1} (compare Tables II and III) is still sizable. A similar attempt to estimate anharmonicity effects for the other two vibrational modes in $[Ar-N_2]^{+\cdot}$ was not attempted because, in view of their having quite similar wavelengths, they are likely to show strong coupling effects. These are neglected in our approach. The DFT harmonic values for the ν_{N-N} mode in $[Ar-N_2]^{+\cdot}$ (see Table S3) are roughly 50 cm^{-1} smaller than the harmonic CCSD(T)/cc-pVQZ value and are thus already closer to the experimental values than the CCSD(T) harmonic results. This suggests that adding an anharmonic correction would bring the DFT frequencies into very close agreement with the experimentally measured frequency. The various methods used to com-

TABLE I. The experimentally observed rovibrational transitions of the charge-transfer complex $[Ar-N_2]^{+\cdot}$ in its $^2\Sigma$ electronic ground state upon vibrational excitation of the NN stretch. The assignment is given for the two spin rotation progressions $F_1(N,J)$ and $F_2(N,J)$ as defined in the text. All values are given in cm^{-1}.

N	J	P_1 branch	$(o\text{-}c)$ (10^{-4})	R_1 branch	$(o\text{-}c)$ (10^{-4})	N	J	P_2 branch	$(o\text{-}c)$ (10^{-4})	R_2 branch	$(o\text{-}c)$ (10^{-4})
0	1/2	⋯	⋯	2272.5082	8	1	1/2	⋯	⋯	2272.7727	−6
1	3/2	2272.0043	1	2272.7634	5	2	3/2	2271.7359	9	2273.0279	3
2	5/2	2271.7460	1	2273.0178	5	3	5/2	2271.4762	6	2273.2810	0
3	7/2	2271.4866	1	2273.2711	3	4	7/2	2271.2150	−2	2273.5334	1
4	9/2	2271.2256	−6	2273.5233	1	5	9/2	2270.9537	−1	2273.7853	6
5	11/2	2270.9649	0	2273.7752	6	6	11/2	2270.6912	−2	2274.0345	−5
6	13/2	2270.7032	6	2274.0240	−11	7	13/2	2270.4275	−5	2274.2844	0
7	15/2	2270.4391	−2	2274.2742	−3	8	15/2	2270.1637	1	2274.5332	5
8	17/2	2270.1751	1	2274.5229	0	9	17/2	2269.8986	4	2274.7806	6
9	19/2	2269.9106	9	2274.7705	2	10	19/2	2269.6307	−12	2275.0267	4
10	21/2	2269.6429	−6	2275.0165	−2	11	21/2	2269.3635	−11	2275.2710	−5
11	23/2	2269.3757	−6	2275.2612	−9	12	23/2	2269.0952	−11	2275.5160	2
12	25/2	2269.1073	−8	2275.5062	−2	13	25/2	2268.8261	−10	2275.7592	2
13	27/2	2268.8384	−5	2275.7493	−5	14	27/2	2268.5562	−6	2276.0024	11
14	29/2	2268.5682	−6	2275.9922	1	15	29/2	2268.2857	1	2276.2425	1
15	31/2	2268.2986	9	2276.2324	−10	16	31/2	2268.0131	−4	2276.4822	−4
16	33/2	2268.0258	2	2276.4725	−11	17	33/2	2267.7382	−21	2276.7208	−10
17	35/2	2267.7516	−10	2276.7118	−11	18	35/2	2267.4687	24	2276.9586	−13
18	37/2	2267.4811	25	2276.9495	−16	19	37/2	2267.1924	12	2277.1984	14
19	39/2	2267.2051	14	2277.1904	21	20	39/2	2266.9163	11	2277.4343	13
20	41/2	2266.9284	7	2277.4258	14	21	41/2	⋯	⋯	2277.6689	8
21	43/2	⋯	⋯	2277.6599	3	22	43/2	2266.3593	−10	2277.9023	2
22	45/2	2266.3720	−11	2277.8943	6	23	45/2	2266.0824	9	2278.1341	−9
23	47/2	2266.0949	6	2278.1253	−14	24	47/2	2265.8007	−10	⋯	⋯
24	49/2	2265.8139	−7	⋯	⋯	25	49/2	2265.5214	5	⋯	⋯
25	51/2	2265.5339	0	⋯	⋯	26	51/2	2265.2382	−10	⋯	⋯
26	53/2	2265.2526	3	⋯	⋯	⋯	⋯	⋯	⋯	⋯	⋯

J	Q_{12}	$o\text{-}c$ (10^{-4})	Q_{21}	$o\text{-}c$ (10^{-4})
1/2	2272.5212	−21	2271.9909	27

pute infrared intensities all point to a ratio of ca. $3:1:\sim 0$ for N–N stretch:Ar–N stretch:bending (see Table S4). There are, however, significant differences between the methods regarding absolute intensity values.

Our benchmark results, CCSD(T)/cc-pV(Q5)Z, for the binding energies are in excellent agreement with experiment (see Table III). We find a binding energy for $Ar+N_2^{+\cdot}$ of −28.2 kcal/mol (including ZPE), while the experimental number is −28 kcal/mol.[53] Furthermore, we find that, at CCSD(T)/cc-pV(Q5)Z, the binding energy between the alternative fragments $Ar^{+\cdot}+N_2$ lies 4.05 kcal/mol higher in energy than for $Ar+N_2^+$ [in this value, the spin-orbit coupling term of −1.4150 kcal/mol for $Ar^{+\cdot}(^2P_{3/2})$ has been taken into account]. This is again in excellent agreement with the corresponding experimental energy difference of 4.3 kcal/mol. All DFT methods used are also able to reproduce the right energetic order (i.e., $Ar+N_2^{+\cdot}$ more stable than $Ar^{+\cdot}+N_2$) but they yield overbinding by 10–15 kcal/mol for the GGAs [and up to 23 kcal/mol for LDA]. This is a rather large error that has been attributed to a well-known deficiency[54] of the existing exchange-correlation functionals to properly cancel the self-interaction part of the Coulomb energy in case of delocalized ionization out of symmetry equivalent weakly (or non-) overlapping orbitals {i.e., the Ar $3p_\sigma$ AO and the $N_2^{+\cdot}$ $3\sigma_g$ discussed in Sec. III B 3 [Although the overlap of ca. 0.15 (see Table IV) is strong for a $2c$-$3e$ bond, it is still weak in the sense that it leads to the manifestation of the deficiency in the exchange-correlation functional mentioned in Sec. III B 1.]}. While this particular deficiency of the exchange functionals should be kept in mind, it does not hamper our qualitative analysis of the bonding mechanism.

TABLE II. The experimentally determined molecular parameters of the charge-transfer complex $[Ar-N_2]^{+\cdot}$ in its $^2\Sigma$ electronic ground state for the $v=0$ and NN-excited ($v=1$) state. All values are given in cm^{-1}.

	ν	B_v	D_v (10-8)	γ_v
$v=0$	0	0.128701(8)	7.8(9)	−0.01067(19)
$v=1$	2272.2563(2)	0.128203(8)	7.7(9)	−0.01057(19)

2. EFGs and NQCCs

Our calculated electric-field gradients can be found in Table III. The EFG on Ar has quite a large value, 4.9973 a.u. However, Ar does not pose a nuclear quadrupole moment, so

TABLE III. Benchmark CCSD(T) spectroscopic constants and molecular parameters.

Geometry-related data (in Å or cm^{-1})		
R_e(Ar–N)=2.190	R_e(N–N)=1.102	B_e=0.12750
Bond energies (in kcal/mol)[a]		
$\Delta E(Ar+N_2^{+\cdot})=-28.2$	$\Delta E(Ar^{+\cdot}+N_2)=-32.2$	
Vibrational frequencies (in cm^{-1})[b]		
$\nu_{N-N}^{harm}=2408.2$[b]	$\nu_{N-Ar}^{harm}=337.9$	$\nu_{bend}^{harm}=83.2$
$\nu_{N-N}^{anharm}=2334.5$[c]		
Electric-field gradients (in a.u.)		
q(Ar)=4.9973	$q(N_c)=-0.3268$	$q(N_t)=-0.9535$
Nuclear quadrupole coupling constants (in MHz)		
NQCC(Ar)=0[d]	NQCC(N_c)=−1.569[e]	NQCC(N_t)=−4.579[e]

[a]Binding energies ΔE have been corrected for zero-point vibrational energy effects.
[b]This harmonic value corresponds to the one calculated using the cc-pVQZ basis set (see Sec. II B 2).
[c]The anharmonic value corresponds to the one calculated using the cc-pVQZ basis set (see Sec. II B 2).
[d] ^{40}Ar has no nuclear quadrupole moment.
[e]Calculated using the nuclear quadrupole moment of 20.44(3) mbarn for ^{14}N from Ref. 31.

the nuclear quadrupole couplings constant is zero. The EFGs on the nitrogen atoms are quite small, −0.3268 a.u. for the central N atom (N_c) and −0.9535 a.u. for the terminal N atom (N_t). The nuclear quadrupole couplings constants on N_c and N_t are −1.569 and −4.579 MHz, respectively.

3. Ar–N bonding mechanism

Our analyses reveal that the Ar–N bond in $[Ar-N_2]^{+\cdot}$ is a textbook example of a classical 2-center-3-electron ($2c$-$3e$) bond. Here, we focus on the results obtained at the BP86/TZ2P level of the generalized-gradient approximation to DFT, using the CCSD(T)/cc-pVQZ geometry (see Table IV and Fig. 3) and we have verified that exactly the same picture emerges at other levels of theory, i.e., LDA, BLYP, and OLYP (see Tables S6–S9). In Fig. 3 the frontier orbital interactions between the Ar atom and molecular nitrogen radical cation are schematically shown. The numbers at the dashed lines are Gross Mulliken contributions of the fragment orbitals to the overall $[Ar-N_2]^{+\cdot}$ molecular orbitals; they serve to provide a semiquantitative picture of the Ar–N orbital interactions. The main feature is the three-electron bonding interaction between the "closed-shell" Ar $3p_\sigma$ atomic orbital (AO) and the $N_2^{+\cdot}$ $3\sigma_g$ singly occupied molecular orbital (SOMO). These two fragment orbitals strongly mix and interact because of their closeness in energy (as reflected also by the minimal difference in ionization energy

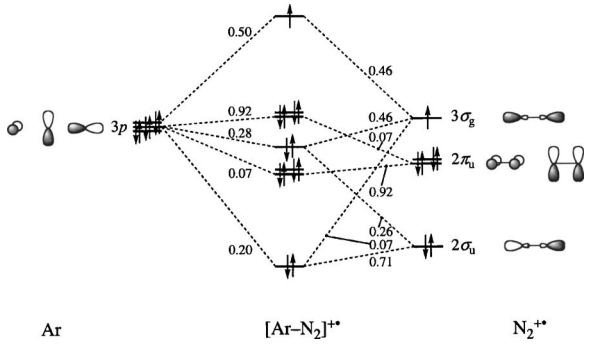

FIG. 3. Schematic diagram for the orbital interactions between Ar and $N_2^{+\cdot}$ in $[Ar-N_2]^{+\cdot}$.

TABLE IV. Analysis of the Ar–N bond in $[Ar-N_2]^{+\cdot}$ and $[Ar-N_2]$ computed at BP86/TZ2P.

	$[Ar-N_2]^{+\cdot}$		$[Ar-N_2]$[a]
	$Ar+N_2^{+\cdot}$	$Ar^{+\cdot}+N_2$	$Ar+N_2$
Bond energy decomposition (in kcal/mol)			
ΔV_{elst}	−11.30	−18.72	−22.88
ΔE_{Pauli}	41.90	38.27	62.92
ΔE_{oi}	−75.67	−71.83	−7.63
ΔE_σ	−70.79	−65.44	−5.48
ΔE_π	−4.88	−6.40	−2.15
ΔE_{int}	−44.98	−52.28	32.41
ΔE_{prep}	0.16	0.00	0.00
ΔE	−44.82	−52.28	32.41
Fragment orbital overlap			
$\langle Ar-3p_z \vert N_2-3\sigma_g\rangle$	0.153	0.143	0.167
Fragment orbital populations (in electrons)			
Ar: $3p_z$	1.46	1.48	1.99
$3p_x+3p_y$	3.96	3.96	3.98
N_2: $2\sigma_u$	1.98	1.98	2.00
$3\sigma_g$	1.54	1.53	1.96
$1\pi_u$	4.00	4.00	4.00
Atomic charges (in a.u.)[b]			
Ar	0.512 (0.523)	0.512 (0.523)	−0.002 (0.010)
N_c	0.203 (0.207)	0.203 (0.207)	0.009 (−0.002)
N_t	0.284 (0.270)	0.284 (0.270)	−0.007 (−0.008)

[a]Analyses for neutral $[Ar-N_2]$ were carried out at the equilibrium geometry of $[Ar-N_2]^{+\cdot}$.
[b]VDD Refs. 48 and 49 and, in parentheses, Hirschfeld (Refs. 49 and 50) atomic charges.

of Ar and N_2) and because they achieve a relatively large overlap of 0.153. Note that the latter is in fact close to the optimal overlap value of 0.17 for a three-electron bond between two initially degenerate fragment orbitals in simple Hückel theory with overlap.[55,56]

As pointed out earlier for the $[H_2S-H_2S]^{+\cdot}$ complex,[57] the three-electron Ar–N bond can be conceived as a one-electron bond, providing the main contribution to the stabilizing orbital interaction term ΔE_{oi} of −75.7 kcal/mol, plus a 2-same-spin-electron repulsive interaction, providing the main contribution to the Pauli-repulsion term ΔE_{Pauli} of 41.9 kcal/mol. The one-electron bond occurs between, say, the β electron in the $3p_\sigma\beta$ spin-orbital of Ar and the empty $3\sigma_g\beta$ spin-orbital of $N_2^{+\cdot}$ whereas the Pauli-repulsive component arises between corresponding α spin-orbitals which are both occupied. (See also Ref. 58 for the orbital electronic structure of $N_2^{+\cdot}$ versus that of N_2.) Essentially the same picture (with only slightly different numerical details) arises if the Ar–N bond is analyzed in terms of the slightly higher-energy fragments $Ar^{+\cdot}+N_2$ instead of $Ar+N_2^{+\cdot}$ (see Table IV). The symmetric character of the three-electron Ar–N bond and the near degeneracy of the two alternative fragmentation pathways agree well with the atomic charge analysis. Both, VDD and Hirshfeld atomic charges show that the net positive charge is nearly perfectly delocalized over the argon and nitrogen fragments: $Q(Ar)=+0.512$ and +0.523 a.u., respectively (see Table IV).

Our bond analyses also shed new light on the role of charge in the Ar–N bond in $[Ar-N_2]^{+\cdot}$. It is commonly believed that the substantial increase in Ar–N bond strength if one goes from the neutral van der Waals complex $[Ar-N_2]$ to the radical cation complex $[Ar-N_2]^{+\cdot}$ is associated with the introduction of a charge, suggesting increased electrostatic attraction. However, the main source of electrostatic attraction between two neutral or between a neutral and a charged fragment is the stabilization that occurs as electronic charge density of one fragment overlaps with the nuclei of the other fragment.[46] This electrostatic stabilization does not change dramatically if one removes, for example, an electron from one of two neutral fragments. To demonstrate this for the present situation, we have also analyzed the Ar–N bond of the neutral $[Ar-N_2]$ complex at the equilibrium geometry of $[Ar-N_2]^{+\cdot}$. The results are also collected in Table IV. From $[Ar-N_2]^{+\cdot}$ to $[Ar-N_2]$ the "bond energy" goes from −44.8 kcal/mol stabilizing to +32.4 kcal/mol repulsive, i.e., it becomes 77.2 kcal/mol less stabilizing. This is not unexpected because the equilibrium Ar–N bond distance of 2.190 of $[Ar-N_2]^{+\cdot}$ is located on the repulsive wall of the weakly bound van der Waals complex $[Ar-N_2]$ which has a significantly longer equilibrium Ar–N distance. Note, however, that this is not due to a decrease in electrostatic attraction ΔV_{elstat} which in fact becomes even *more* attractive, although only by 11.6 kcal/mol. The main reason for the destabilization is the loss of the three-electron bond or, to be more precise, the loss of the one-electron bonding component therein. This component is substituted in $[Ar-N_2]$ by a second Pauli-repulsive 2-orbital 2-same-spin-electron repulsion. Thus, overall, adding an electron to $[Ar-N_2]^{+\cdot}$ causes the three-electron *bond* to turn into two lone pairs having Pauli repulsion (cf. "4-electron destabilizing interaction"). This translates into a nearly complete extinction of the orbital interactions ΔE_{oi}, from −75.7 to −7.6 kcal/mol, and a substantial increase of the Pauli repulsion, from +41.9 to +62.9 kcal/mol. It is, in conclusion, more correct to attribute the increased stability of $[Ar-N_2]^{+\cdot}$ to its radical character than to its charge.

IV. CONCLUSION

New experimental and theoretical results have been obtained that allow a detailed description of the molecular properties of the charge-transfer complex $[Ar-N_2]^{+\cdot}$. Spectroscopic results are summarized in Tables I and II and the outcome of high-level calculations is given in Tables III and IV. Additional detailed information is available from Ref. 59. The combined study provides accurate information on molecular geometry and allows a detailed study of the electronic structure and the bonding mechanism. The complex is produced relatively easily in Ar/N_2 plasma and as such it may be interesting as a benchmark molecule for characterizing plasma features. The detailed spectroscopic constants, in addition, may be used to guide a detailed microwave study of this complex.

ACKNOWLEDGMENTS

The authors thank Dr. J. Neugebauer for useful discussions. One of the authors (D.V.) acknowledges EU support within the integrating infrastructure initiative; Contract No. RII3-CT-2003-506350 (LCVU Access program). The Netherlands Organization for Scientific Research (NWO) and the Dutch organization for Fundamental Research (FOM) are acknowledged for financial support. The Laser Centre of the Free University Amsterdam (LCVU) and Professor Dr. W. van der Zande and Dr. W. L. Meerts of the Department of Molecule and Laser Physics of the University of Nijmegen are thanked for substantial instrumental support.

[1] E. J. Bieske and O. Dopfer, Chem. Rev. (Washington, D.C.) **100**, 3963 (2000).
[2] S. A. Nizkorodov, Y. Spinelli, E. J. Bieske, J. P. Maier, and O. Dopfer, Chem. Phys. Lett. **265**, 303 (1997).
[3] O. Dopfer, R. V. Olkhov, and J. P. Maier, J. Phys. Chem. **103**, 2982 (1999).
[4] P. Botschwina, R. Oswald, H. Linnartz, and D. Verdes, J. Chem. Phys. **113**, 2736 (2000).
[5] E. J. Bieske and J. P. Maier, Chem. Rev. (Washington, D.C.) **93**, 2603 (1993).
[6] H. Linnartz, D. Verdes, and T. Speck, Rev. Sci. Instrum. **71**, 1811 (2000).
[7] D. Verdes, H. Linnartz, J. P. Maier, P. Botschwina, R. Oswald, P. Rosmus, and P. J. Knowles, J. Chem. Phys. **111**, 8400 (1999).
[8] H. Linnartz, D. Verdes, P. J. Knowles, N. M. Lakin, P. Rosmus, and J. P. Maier, J. Chem. Phys. **113**, 895 (2000).
[9] K. M. Weitzel and J. Maehnert, Int. J. Mass Spectrom. Ion Process. **214**, 175 (2002).
[10] H. S. Kim and M. T. Bowers, J. Chem. Phys. **93**, 1158 (1990).
[11] H. Linnartz, D. Verdes, and J. P. Maier, Science **297**, 1166 (2002).
[12] T. Helgaker, P. Jørgensen, and J. Olsen, *Molecular Electronic Structure Theory* (Wiley-VCH, Chichester, 2000).
[13] R. G. Parr and W. Yang, *Density-functional Theory of Atoms and Molecules* (Oxford University Press, New York, 1989).
[14] W. Koch and M. C. Holthausen, *A Chemists's Guide to Density Functional Theory* (Wiley-VCH, Weinheim, 2000).

[15] D. Kauer, A. M. de Souza, J. Wanna, S. A. Hammad, L. Mercorelli, D. S. Perry, Appl. Opt. **29**, 119 (1990).
[16] H. Linnartz, Phys. Scr. **70**, C24 (2004).
[17] T. P. Straatsma, E. Apra, T. L. Windus *et al.*, NWCHEM, A computational chemistry package for parallel computers, Version 4.6, Pacific Northwest National Laboratory, Richland, Washington 99352-0999, USA, 2004.
[18] T. H. Dunning, Jr., J. Chem. Phys. **90**, 1007 (1989).
[19] D. E. Woon and T. H. Dunning, Jr., J. Chem. Phys. **98**, 1358 (1993).
[20] R. A. Kendall, T. H. Dunning, Jr., and R. J. Harrison, J. Chem. Phys. **96**, 6796 (1992).
[21] D. E. Woon and T. H. Dunning, Jr., J. Chem. Phys. **100**, 2975 (1994).
[22] H. J. Aa. Jensen, T. Saue, L. Visscher *et al.*, DIRAC, a relativistic *ab initio* electronic structure program, release DIRAC04.0, 2004; http://dirac.chem.sdu.dk
[23] K. G. Dyall, J. Chem. Phys. **100**, 2118 (1994).
[24] L. Visscher, E. Eliav, and U. Kaldor, J. Chem. Phys. **115**, 9720 (2001).
[25] D. A. Clabo, W. D. Allen, R. B. Remington, Y. Yamaguchi, and H. F. Schaefer III, Chem. Phys. **123**, 187 (1988).
[26] W. Schneider and W. Thiel, Chem. Phys. Lett. **157**, 367 (1989).
[27] J. Neugebauer and B. A. Hess, J. Chem. Phys. **118**, 7215 (2003).
[28] A. Halkier, H. Koch, O. Christiansen, P. Jørgensen, and T. Helgaker, J. Chem. Phys. **107**, 849 (1997).
[29] J. N. P. van Stralen and L. Visscher, J. Chem. Phys. **117**, 3103 (2002).
[30] P. Pyykkö, Mol. Phys. **99**, 1617 (2001).
[31] G. te Velde *et al.*, J. Comput. Chem. **22**, 931 (2001).
[32] S. H. Vosko, L. Wilk, and M. Nusair, Can. J. Phys. **58**, 1200 (1980).
[33] H. Stoll, C. M. E. Pavlidou, and H. Preuss, Theor. Chim. Acta **49**, 143 (1978).
[34] A. D. Becke, Phys. Rev. A **38**, 3098 (1988).
[35] J. P. Perdew, Phys. Rev. B **33**, 8822 (1986).
[36] C. Lee, W. Yang, and R. G. Parr, Phys. Rev. B **37**, 785 (1988).
[37] J. P. Perdew, J. A. Chevary, S. H. Vosko, K. A. Jackson, M. R. Pederson, D. J. Singh, and C. Fiolhais, in *Electronic Structure of Solids '91*, edited by P. Ziesche and H. Eschrig (Akademie, Berlin, 1991), Vol. 17.
[38] J. P. Perdew *et al.*, Phys. Rev. B **46**, 6671 (1992).
[39] J. P. Perdew, K. Burke, and M. Ernzerhof, Phys. Rev. Lett. **77**, 3865 (1996).
[40] J. P. Perdew, K. Burke, and M. Ernzerhof, Phys. Rev. Lett. **78**, 1396 (1997).
[41] Y. Zhang and W. Yang, Phys. Rev. Lett. **80**, 890 (1998).
[42] N. C. Handy and A. J. Cohen, Mol. Phys. **19**, 403 (1970).
[43] C. Adamo and V. Barone, J. Chem. Phys. **108**, 664 (1998).
[44] T. Ziegler and A. Rauk, Theor. Chim. Acta **46**, 1 (1977).
[45] F. M. Bickelhaupt, N. M. M. Nibbering, E. M. van Wezenbeek, and E. J. Baerends, J. Phys. Chem. **96**, 4864 (1992).
[46] F. M. Bickelhaupt and E. J. Baerends, in *Reviews in Computational Chemistry*, edited by K. B. Lipkowitz and K. B. Boyd (Wiley-VCH, New York, 2000), Vol. 15, p. 1.
[47] E. J. Baerends, D. E. Ellis, and P. Ros, Chem. Phys. **2**, 41 (1973).
[48] F. M. Bickelhaupt, N. J. R. van Eikema Hommes, C. Fonseca Guerra, and E. J. Baerends, Organometallics **15**, 2923 (1996).
[49] C. Fonseca Guerra, J. W. Handgraaf, E. J. Baerends, and F. M. Bickelhaupt, J. Comput. Chem. **25**, 189 (2004).
[50] F. L. Hirshfeld, Theor. Chim. Acta **44**, 129 (1977).
[51] C. M. Western, PGOPHER v3, School of Chemistry, University of Bristol, England, 1994.
[52] T. Ruchti, T. Speck, J. P. Connelly, E. J. Bieske, H. Linnartz, and J. P. Maier, J. Chem. Phys. **105**, 2591 (1996).
[53] J. Maehnert, H. Baumgaertel, and K.-M. Weitzel, J. Chem. Phys. **102**, 180 (1995).
[54] M. Grüning, O. V. Gritsenko, S. J. A. van Gisbergen, and E. J. Baerends, J. Phys. Chem. A **105**, 9211 (2001).
[55] N. C. Baird, J. Chem. Educ. **54**, 291 (1977).
[56] P. M. Gill and L. Radom, J. Am. Chem. Soc. **110**, 4931 (1988).
[57] F. M. Bickelhaupt, A. Diefenbach, S. P. de Visser, L. J. de Koning, and N. M. M. Nibbering, J. Phys. Chem. A **102**, 9549 (1998).
[58] F. M. Bickelhaupt, R. Hoffmann, and R. D. Levine, J. Phys. Chem. A **101**, 8255 (1997).
[59] See EPAPS Document No. E-JCPSA6-123-005534 for supplementary material containing detailed information on the theoretical part of this work. This document can be reached via a direct link in the online article's HTML reference section or via the EPAPS homepage (http://www.aip.org/pubservs/epaps.html).